ADVANCED MATERIALS TECHNOLOGIES
www.advmattechnol.de

Thermomechanical Soft Actuator for Targeted Delivery of Anchoring Drug Deposits to the GI Tract

*Joshua A. Levy, Michael A. Straker, Justin M. Stine, Luke A. Beardslee, Vivian Borbash, and Reza Ghodssi**

Current systemic therapies for inflammatory gastrointestinal (GI) disorders are unable to locally target lesions and have substantial systemic side effects. Here, a compact mesoscale spring actuator capable of delivering an anchoring drug deposit to point locations in the GI tract is demonstrated. The mechanism demonstrated here is intended to complement existing ingestible capsule-based sensing and communication technologies, enabling treatment based on criteria such as detected GI biomarkers or external commands. The 3D-printed actuator has shown on command deployment in 14.1 ± 3.0 s, and a spring constant of 25.4 ± 1.4 mN mm^{-1}, sufficient to insert a spiny microneedle anchoring drug deposit (SMAD) into GI tissue. The complementary SMAD showed a 22-fold increase in anchoring force over traditional molded microneedles, enabling reliable removal from the actuator and robust prolonged tissue attachment. The SMAD also showed comparable drug release characteristics (R^2 = 0.9773) to penetrating molded microneedles in agarose phantom tissue with a drug spread radius of 25 mm in 168 h. The demonstrated system has the potential to enable on command delivery and anchoring of drug-loaded deposits to the GI mucosa for sustained treatment of GI inflammation while mitigating side effects and enabling new options for treatment.

1. Introduction

Inflammatory bowel disease (IBD), that is, Crohn's disease and ulcerative colitis (UC) is a class of inflammatory gastrointestinal (GI) disorder that impacts 3.1 million adults in the United States and involves chronic inflammation and eventual damage of the gastrointestinal tract.[1–3] Conventional treatment for inflammatory bowel disease (IBD) is primarily achieved through oral or intravenous delivery of therapeutic agents.[4,5] A wide variety of drugs can be employed, including aminosalicylic acids, corticosteroids, immunosuppressants, and various biological macromolecules.[6–8] These medications have a myriad of adverse side effects, limiting the course of treatment for patients.[9–11] For example, corticosteroid treatment duration is limited to approximately 3 months to mitigate the potential for conditions like osteoporosis,[12,13] and immunosuppressants increase susceptibility to opportunistic infections.[14] The presence of substantial side effects can be partly attributed to the large systemic doses needed to achieve effective therapeutic concentrations within the GI tract. Localizing treatment to inflammatory lesions using topically active agents, like corticosteroids, is one method to reduce the necessary drug dose and combat the adverse systemic side effects associated with intravenous and oral non-site-specific therapeutic delivery.[13,15–17] Highly localized topical treatment may also offer a path to mitigate drug costs by reduced dosing, making room for costs associated with innovative delivery modalities.

Commercial technologies exist that can improve the localization of drug release within the GI tract. One such technology is pH-sensitive enteric coatings, like Evonik Eudragit L100,

J. A. Levy, R. Ghodssi
Department of Materials Science and Engineering
University of Maryland
College Park, MD 20742, USA
E-mail: ghodssi@umd.edu

The ORCID identification number(s) for the author(s) of this article can be found under https://doi.org/10.1002/admt.202201365.

DOI: 10.1002/admt.202201365

J. A. Levy, M. A. Straker, J. M. Stine, L. A. Beardslee, V. Borbash, R. Ghodssi
Institute for Systems Research
University of Maryland
College Park, MD 20742, USA

J. A. Levy, M. A. Straker, J. M. Stine, R. Ghodssi
Robert E. Fischell Institute for Biomedical Devices
University of Maryland
College Park, MD 20742, USA

M. A. Straker, R. Ghodssi
Fischell Department of Bioengineering
University of Maryland
College Park, MD 20742, USA

J. M. Stine, V. Borbash, R. Ghodssi
Department of Electrical and Computer Engineering
University of Maryland
College Park, MD 20742, USA

that swell and release drugs in pH-specific regions in the GI tract (stomach [pH 1.5–3], small intestine [pH 6–7.4], caecum [pH 5.7], etc.).[18,19] Such coatings help to localize delivery; either focusing the release of systemic drugs to the most absorbent regions of the GI tract or releasing locally active drugs in the most afflicted GI regions enabling site-specific treatment. Another technology that can be applied in conjunction with pH-sensitive polymers is mucoadhesive coatings.[5,20] These coatings bind to the intestinal mucus layer via valence forces or interlocking action slowing tablet transit; thus, localizing the release and delivery of the contained therapeutics.[21] Both technologies help to localize to regions in the GI tract, but do not allow the targeting of highly specific locations of disease affliction. Furthermore, the physiological attributes that determine localization (pH and mucus) can vary from patient to patient.

With the advancement of microsystem fabrication technology enabling the miniaturization of remote electronics, sensors and actuators, the treatment of diseases within isolated locations in the human body has become more attainable. Recently, a focus of many researchers on ingestible capsule devices has enabled drug delivery to several regions within the GI tract to treat systemic diseases.[22] For example, the spring-loaded SOMA capsule can deliver millimeter-scale dissolving needles to the stomach triggered by hydration-dependent polymers,[23] and the Rani Pill can do the same using pH-responsive polymers.[24] The LUMI capsule also uses a pH-responsive unfolding mechanism to inject microneedle patches into small intestine tissue.[25] While these passive mechanisms support locational delivery, they do not permit fully closed-loop deployment in response to sensors or explicit commands, and hence only offer regional control over delivery.

Sensing technologies such as optical sensing,[26] gas sensing,[27–29] pH sensing,[30] temperature sensing,[31] and electrochemical impedance spectroscopy (EIS)[32] have been readily integrated into ingestible capsules in recent years. These sensing modalities can give insights into the current state of inflammation in the GI tract and be used to inform active targeted drug delivery to afflicted tissue locations. However, due to the motion in the GI tract, rapid on command actuation is a key requirement to feedback-driven localized therapeutic treatment. Previously, MEMS-based actuators have been developed to achieve on command payload release in ingestible fluid drug delivery and endoscopic location tagging capsules.[33] Various investigators have employed heating elements[34,35] and combustion-based microthrusters[36,37] to achieve a rapid release of fluid drugs from a reservoir. Goffredo et al. even integrated a ring electrode electrochemical impedance spectroscopy (EIS) sensor with a fluid drug release reservoir.[38] Yet, localization using this fluid payload release method is limited due to fluid dispersion after release from the capsule reservoir, which varies by case and allows little opportunity for control over the release profile. An alternative method capable of further localizing delivery of therapeutics in the GI tract is active delivery of drug-loaded dissolving microneedles to the GI tissue. Lee et al. demonstrated this type of site-specific microneedle delivery using a magnetic locomotion and actuation system.[39] Though they were able to achieve highly localized delivery ex vivo, utilizing such a system in vivo requires external electromagnetic devices that may be clinically impractical. Furthermore, Lee and co-authors observed challenges with tissue adherence of the therapeutic-loaded molded microneedles. A variety of passive and active microsystems have been used previously to enable tissue attachment by latching on to tissue with different forms of thermo and hydration responsive microgrippers,[40] theragrippers,[41,42] microinjectors,[43] and anchoring microneedles[44–48] on benchtop and in vivo. The tissue attachment achieved using these technologies enables long-term residency for extended-release therapeutic delivery, however locational control is still limited. Various forms of thermoresponsive soft meso-scale actuators are also prevalent in literature,[49–51] however the application of these systems for ingestible capsule-based localized drug delivery has yet to be demonstrated. Furthermore, a true combination of thermally triggered and highly localized actuation with active or passive anchoring techniques remains elusive and is a powerful coupling for achieving superlative control over drug localization and release.

In this paper, we look to address the challenges of site-specific and on command drug delivery in the GI tract (**Figure 1**a) using a thermomechanical spring actuator paired with a biomimetic drug anchoring structure, termed the spiny microneedle anchoring drug deposit (SMAD). The compact system shown in Figure 1 and Figure S1, Supporting Information, is compatible with sensing and communication ingestible capsule technology for closed-loop detection and therapeutic delivery to lesions in the GI tract. Release of a dissolving drug-loaded deposit anchored in the GI tissue allows prolonged delivery of therapeutics in the target region. A novel 3D-printable spring was designed to imitate a wave spring, which is used in applications requiring large travel distance with less consumed space—a necessity for ingestible capsule devices. In addition, this type of spring provides greater lateral stability when compared to a standard conical coil spring. The spring is fixed in compression using polycaprolactone (T_m = 60 °C), and releases by melting the polycaprolactone using a resistive heating element fabricated on a Kapton substrate. The drug-loaded SMAD in Figure 1b attaches to the top of the spring actuator with a water-soluble polymer to enforce reliable release after actuation. The SMAD exploits recently developed biomimetic barbed microneedle technology that has been demonstrated by our group[44,48] and others[45–47] for improved tissue anchoring. The hybrid system developed here can be combined with sensors to enable on command delivery of a drug-loaded anchoring deposit for early, focused, and prolonged treatment of GI lesions and has the potential to be applied for various other localized treatment applications in the gastrointestinal tract.

2. Experimental Section

2.1. Design and Fabrication of Multi-Coil Spring

Springs were designed using Autodesk Fusion 360 (Autodesk, San Rafael, CA, USA) with a base diameter of 3 mm on center, an outer tip diameter of 2.1 mm, and a height of 8 mm. The conical design had four overlapping coils (two clockwise and two counterclockwise) with a pitch of 2.66 mm, a width of 400 μm, and a thickness of 150 μm. COMSOL Multiphysics

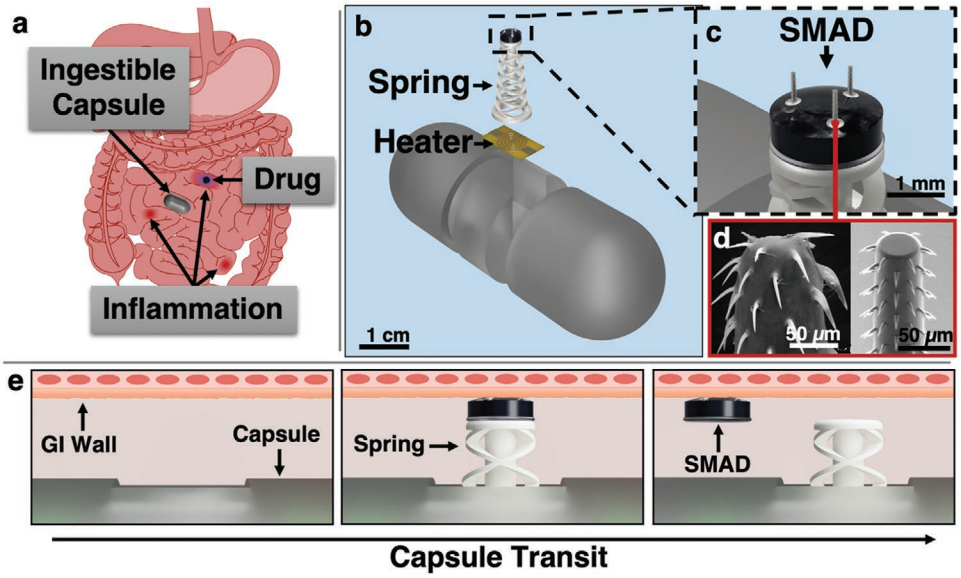

Figure 1. Actuation and SMAD delivery principle. a) Capsule transits through a GI tract with inflammatory lesions and delivers the SMAD to an inflammatory site for prolonged release of a topical therapeutic agent (blue). b) Actuator deployment utilizes a resistive heating element to fire a spring actuator and impart the drug-loaded SMAD into the GI tissue. c) CAD rendering of the SMAD on the actuator. d) Spiny microneedles demonstrated previously[44,48] are designed to mimic a spiny-headed worm proboscis for enhanced anchoring in tissue: Reproduced under terms of the CC-BY license.[52] e) Upon sensed or external command for SMAD delivery, current passes through the heating element, melting the polycaprolactone binder, and firing the spring. The SMAD is then imparted into the tissue and removes as the capsule translates through the intestinal tract.

5.4 (Stockholm, Sweden) was used to compare the overlapping conical springs to a traditional conical coil spring. The single-coil spring was designed with the same 400 μm width as the superimposed spring, however with a 600 μm thickness, 4× that of the superimposed spring, yielding a comparable stiffness. A 50 mN axial force was applied to each spring, and lateral deflection was measured to assess the stability under axial compression/decompression. A 4 mm post (∅ = 1 mm) extends down from the underside of the spring tip to affix compression of the spring with a low melting point PCL polymer (**Figure 2**a).

Springs were fabricated using a Miicraft M50 Digital Light Processing (DLP) 3D printer (CADWorks3D, Concord, ON, Canada) with a 50 μm resolution. Monocure 3D Tuff and Flex 100 resins (Monocure 3D, Regents Park, NSW, Australia) were mixed in 40:60 volume ratio to achieve a balance of flexibility and spring stiffness. An exposure time of 1.5 s per layer was used with a base curing time of 5 s. After printing, the springs were cleaned in isopropyl alcohol for 1 min followed by rinsing with DI water. The springs were then submerged in a DI water bath and UV-cured (405 nm) in a CADWorks3D CureZone (Toronto, ON, Canada) for 10 min at an intensity of 40 mW cm^{-2}. To prevent drying and maintain the elasticity of the polymer, springs were stored in a high humidity chamber until deployment.

2.2. Design and Microfabrication of Resistive Heaters

A resistive heater was designed using Autodesk AutoCAD (San Rafael, CA, USA) for an intended resistance of 50 Ω with a 100 nm thickness of deposited thin-film Au on a 1 mil Kapton polyimide film (McMaster-Carr, Elmhurst, IL, USA). The circular heater coil pattern had an outer diameter of 2.18 mm with trace width of 100 μm and a trace length of 20.6 mm, yielding the theoretical 50 Ω resistance with a Au resistivity of 2.44×10^{-8} Ω·m.[53] The Kapton film, used for its low thermal and electrical conductivities, was mounted to a carrier wafer with 3M double sided tape (St. Paul, MN, USA), then cleaned using acetone, methanol, isopropanol and DI water (18 MΩ). Cr/Au (20 nm/155 nm) was deposited on the surface at ≈2 Å s^{-1} using an Angstrom NexDep Electron Beam Evaporator (Kitchener, ON, Canada) and revealed using a liftoff process.

2.3. Molding of PVA Drug Disk and Microneedle Array

Drug disks were cast from a 20% w/v aqueous solution of polyvinyl alcohol (PVA) (M_w 31–50 kDa, Sigma Aldrich, St. Louis, MO, USA) containing FD&C blue #1 dye. Molding of the drug disks was done by solvent casting of the dye-PVA onto a polystyrene (PS) tray. The casting solution was poured into the container to a depth of 2.5 mm, such that the final film thickness would be 500 μm after the ≈1:5 volume reduction. The solvent was then allowed to evaporate for 24 h in the ambient environment yielding a 500 μm PVA film. The film was peeled from the PS casting tray, and a ∅ = 2 mm punch was used to punch the drug disks from the film.

To form 3 × 3 molded microneedle (MMN) arrays for comparison with the SMAD (Figure S5, Supporting Information), an 11 × 11 microneedle array mold was acquired from Blueacre Technology Ltd. (Dundalk, Co Louth, Ireland). Microneedles molded from the 11 × 11 mold had a height of 600 μm, a base diameter of 300 μm and an interspacing of 600 μm on center. 500 μL of the dye loaded PVA solution was deposited on the

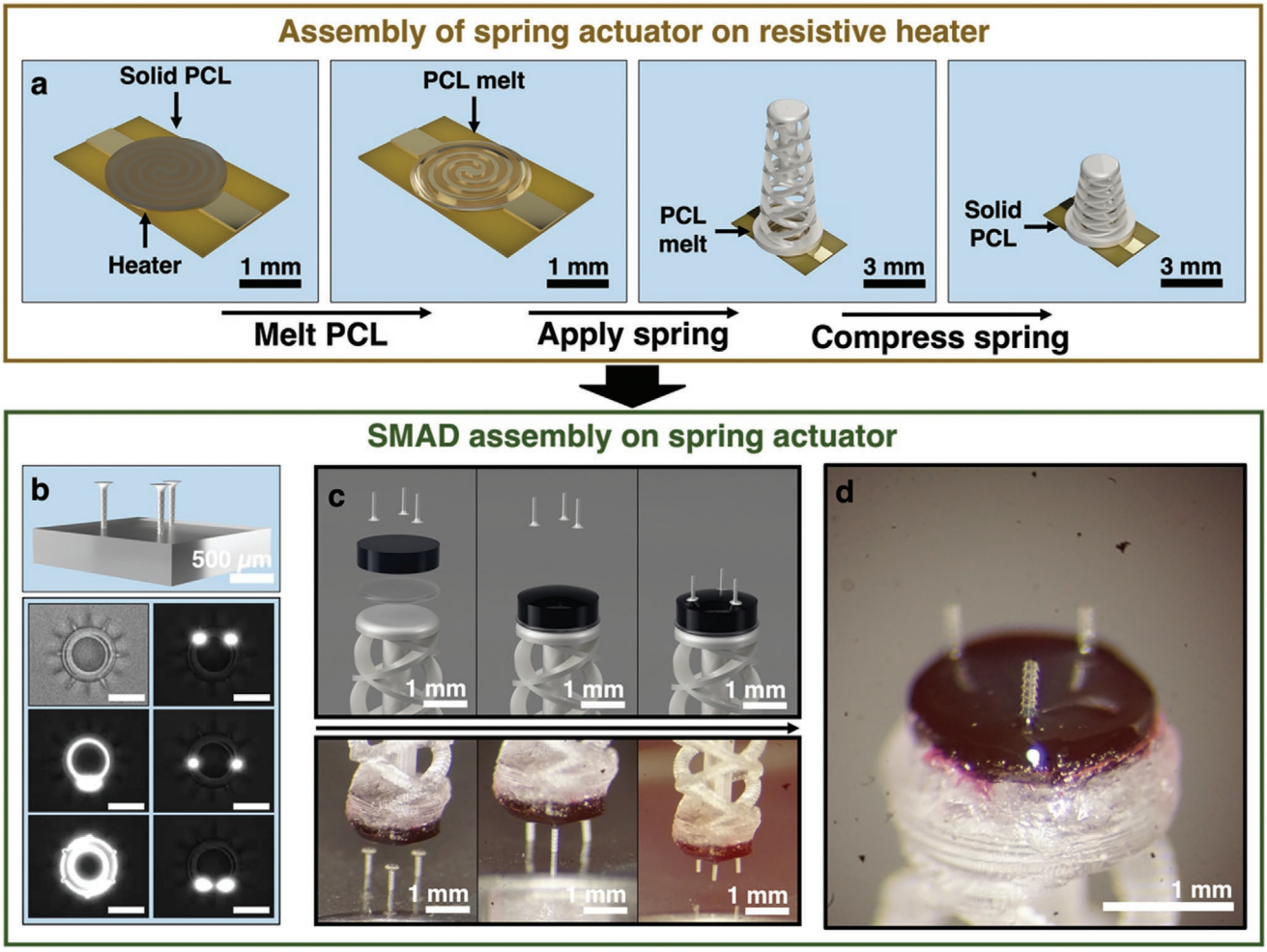

Figure 2. Assembly of the actuator and SMAD structure. a) Assembly of the spring actuator by melting PCL on the resistive heating element then attaching and compressing the spring and solidifying the PCL. b) Computer aided design (CAD) rendering of the inverted triangular pattern of spiny microneedles on the fused silica print substrate and images taken during the photocuring microneedle print process show the hollow shaft structure with attached barbs. The laser scanning pattern can be seen by the illuminated regions that appear in each image during exposure. Unmarked scale bars are 50 µm in length. c) Assembly of the SMAD starting with attachment of the drug disk to the actuator using PEG, followed by attachment of the microneedles to the drug disk, then mechanical removal from the fused silica print substrate. d) Final assembled SMAD structure attached to the actuator with PEG water soluble polymer layer.

microneedle mold, then the mold was placed in vacuum for 15 min to evacuate air from the needle mold, prompting filling of the mold. Molds were then removed from vacuum, and the solvent was allowed to evaporate in the ambient environment for 24 h. Arrays were then segmented into 3 × 3 needle sections.

2.4. Fabrication of Biomimetic Barbed Microneedles

Barbed microneedles previously demonstrated in the authors' group by Liu et al.[44,48] were fabricated by direct laser writing (DLW) (Figure 2b). The microneedles were 650 µm in height with a 74 µm tip diameter and were adapted to include a 300 µm flared base for greater surface contact and enhanced adhesion to the drug disk (Figure S6, Supporting Information). Each needle contains a total of 72 backward-facing barbs with high sharpness (≈1 µm) that promote robust tissue anchoring. DLW was performed using the Dip-in Laser Lithography (DiLL) mode on a fused silica substrate with the Nanoscribe Photonic Professional GT (Karlsruhe, Germany). IP-S photoresist was used with a 25× objective and a slicing distance of 1 µm to fabricate a 3-needle array. Needles were printed upside down in a triangular pattern, each needle being 600 µm from the array center and 120° separated from the adjacent needle. This predetermined spacing supports reliable attachment to the drug disk and control over the spatial arrangement of the needles on the fabricated structure. After printing, needle arrays were cleaned in propylene glycol monomethyl ether acetate (PGMEA) for 15 min, followed by 5 min in isopropyl alcohol and 2 min on a hot plate at 60 °C.

2.5. Package Assembly

Polycaprolactone (PCL) flakes (M_w ≈ 14 000, Sigma Aldrich, St. Louis, MO, USA) were melted and compressed between two Kapton sheets to a thickness of 150 µm. A 4 mm biopsy punch

was used to punch a disk from this film. This disk was melted on top of the resistive heater, then the spring was placed atop the melt, and compressed as shown in Figure 2a. The package was then removed from heat and held compressed until the PCL solidified. The drug disk was then attached to the top of the actuator using ≈1.5 µg of melted polyethylene glycol (PEG) that solidifies after cooling. The assembly was then lowered onto the barbed 3-needle array and adhered using a film of Loctite M-21HP biocompatible (ISO-10993) epoxy adhesive. The adhesive was allowed to cure for 2 h then the assembly was raised to mechanically detach the needles from the fused silica substrate (Figure 2c).

2.6. Mechanical Characterization of Spring Actuator

The spring actuator underwent mechanical compression testing using an Instron 5942 universal testing system (Norwood, MA, USA) equipped with a 10 N load cell. The force profile was obtained during loading and unloading at a crosshead speed of 1 mm min^{-1}. Springs were attached to the platen, then the crosshead was lowered until contacting the spring. Springs were compressed to a displacement of 3 mm, then decompressed until reaching the test origin. Two test groups were evaluated using this protocol: 1) springs compressed for ca. 18 h before testing ($n = 3$); and 2) springs untouched after printing ($n = 8$).

2.7. Characterization of SMAD and MMN Anchoring

Mechanical tests were performed to compare SMAD and MMN tissue anchoring and removal forces (Figure S7, Supporting Information). This was done using the same Instron 5942 universal testing apparatus with a 10 N load cell. All tests were performed using a crosshead speed of 1 mm min^{-1}. Spring actuators fitted with MMN or SMAD tip structures were lowered onto tissue samples until reaching 75 mN of compressive force. Tissue was ordered frozen from Animal Biotech Industries (Boylestown, PA, USA) with mucus attached and without mesentery. Tissue samples were pre-coated with a ≈2 mm layer of 1× phosphate buffered saline solution (PBS) (Sigma Aldrich, St. Louis, MO, USA) to simulate the presence of mucus and aqueous intestinal media on the tissue surface. Upon reaching the 75 mN force, the tissue was moved 2 mm laterally to reproduce the longitudinal motion experienced in the GI tract. The sample was then retracted from the tissue. For samples that removed from the tissue before detaching from the actuator, the tissue removal force was measured. For samples that detached from the actuator and remained in the tissue, the detachment force was measured. An additional group of SMAD samples were permanently adhered to the actuator to determine the SMAD tissue retention force because the SMAD remained anchored in tissue for all other cases.

2.8. Model Drug Delivery

MMN and SMAD samples were compared using a quantitative method to evaluate the diffusion of dye from each structure into agarose phantom tissue. A ≈1 mm agarose film was created in petri dishes, and dye-loaded MMNs and SMADs were applied to the film to evaluate the 2D diffusion profile from each sample type. Images were captured with controlled lighting at set time points from 0 to 168 h after insertion into the agarose phantom. The images were processed in MATLAB R2021b (MathWorks Corporation, Natick, MA, USA) to quantitatively determine the diffusion radius for each time point (Figure S8, Supporting Information). The red channel image was obtained for each image, and the image was binarized using a 40% intensity threshold. Pixels were scaled and counted, and the radius of diffusion was calculated using the number of 0 pixels representing the area of dye spread. Radial diffusion was then plotted, and correction for initial dye mass in each sample was performed in the context of the diffusion equation.

2.9. Deployment Characterization in a Simulated Environment

The heating element, spring actuator, and attached drug disk were packaged in a polyethylene terephthalate glycol (PETG) 3D printed capsule shell to evaluate properties of actuator deployment. Capsules ($n = 7$) were mounted on a custom-made testing apparatus designed to control translation speed of the capsules. Contact was made between the capsule body and an agar hydrogel bed, which was intended to capture the location of contact with the dye-loaded drug disk based on dye remnants in the hydrogel. The capsules were set to translate at 1.4 cm min^{-1} across the hydrogel surface, the mean speed of motion in the small intestine.[54] The actuator was fired at a set displacement along the bed and the deployment translation distance was then measured as the distance between firing the spring actuator and the appearance of the dye marker on the agar bed.

Assessment of the fully assembled SMAD and actuator was performed in a similar manner to the deployment characterizations, however ex vivo porcine intestinal tissue with mucus still attached (Animal Biotech Industries, Boylestown, PA) was used instead of the agar bed. The ex vivo tissue was placed in a 3D-printed PLA semicylindrical cutout (∅ = 25 mm) to replicate the curvature of the small intestine. Test capsules were translated at 1.4 cm min^{-1} and the actuator was deployed via current flow through the resistive heater, and the detachment process of the SMAD from the actuator was monitored. SMAD removal was also evaluated during lateral translation across ex vivo intestinal tissue outside of a capsule to verify removal of the SMAD from the actuator upon capsule translation in the small intestine. The actuator and attached SMAD were lowered onto intestinal tissue (Figure S9, Supporting Information), then the actuator was moved laterally at ≈1.4 cm min^{-1} while monitoring the detachment process via stereomicroscope.

3. Results and Discussion

3.1. Fabrication and Assembly

Figure 2 shows the fabrication and assembly process for the thermomechanical spring actuator and SMAD system. Polycaprolactone (PCL) is melted on the microfabricated resistive heater, then the spring is compressed and held in place when

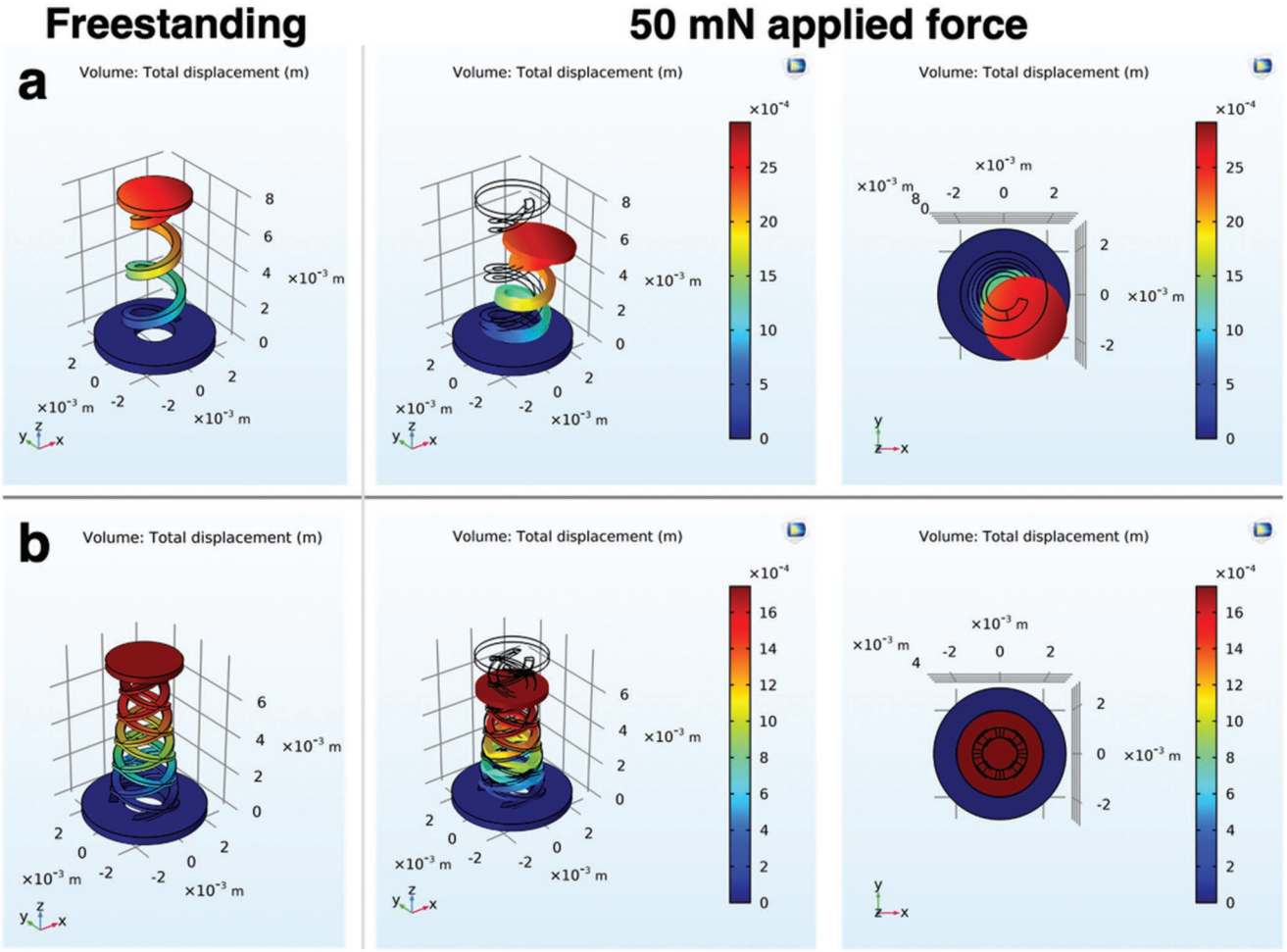

Figure 3. Modelling of spring actuator designs. a) Standard conical coil spring with a coil width of 400 µm, coil height of 600 µm, 3 mm diameter on center, 8 mm height, and 5° inward conical slope. This design showed lateral instability under axial compression with a 1341 µm lateral movement under 50 mN axial compression. b) Wave-like conical spring with 4 overlapping coils with a coil width of 400 µm, coil height of 150 µm, 3 mm diameter on center, 8 mm height, and 5° inward conical slope. This design showed an 87% reduction in lateral perturbations under 50 mN compression due to the four-point contact at the base and tip of the spring.

the PCL solidifies (Figure 2a). The SMAD is then built on top of the spring. First, the biomimetic anchoring microneedles are printed upside down on a fused silica substrate using DLW (Figure 2b). The drug-loaded polyvinyl alcohol (PVA) disk is then attached to the spring with polyethylene glycol (PEG) and the microneedles are transferred to the SMAD via biocompatible epoxy resin (Figure 2c), yielding the fabricated structure (Figure 2d).

3.2. Simulated Characteristics of the 3D-Printed Soft Spring Actuator

Wave springs offer high lateral stability and space conservation in the axial direction, but their fabrication using 3D-printing is challenging due to the low level of connectivity between the stacked coils. To address this challenge, we developed a wave-like spring design that utilizes similar principles to improve lateral stability and axial compression characteristics but is compatible with DLP 3D-printing because of the reinforced joints between coils. **Figure 3** shows a comparison in COMSOL Multiphysics between an 8 mm conical coil spring and the wave-like spring under axial compression with a force of 50 mN. Lateral deflection experienced by the superimposed spring was reduced to approximately 1/8th that of the standard conical coil spring (1341 to 172 µm). This result validates this design, indicating higher stability under axial loading—a necessary attribute for reliable injection of microneedles into the mucosal tissue using a freestanding soft spring actuator. Furthermore, the lateral stability achieved by this design is critical for the repeatable 3D printing of the springs in a vat polymerization process like DLP. Springs with less lateral stability tended to sway with movements of the build plate and resin, causing misalignments between the crosslinked layers, and print failure in some cases. DLP 3D fabrication is advantageous because it permits the fabrication of soft polymeric springs with blunt surfaces and tunable mechanical characteristics by varying the volume ratio of the Tuff:Flex100 resins that were used. The balance of compliance and stiffness achieved here is critical to attaining sufficient

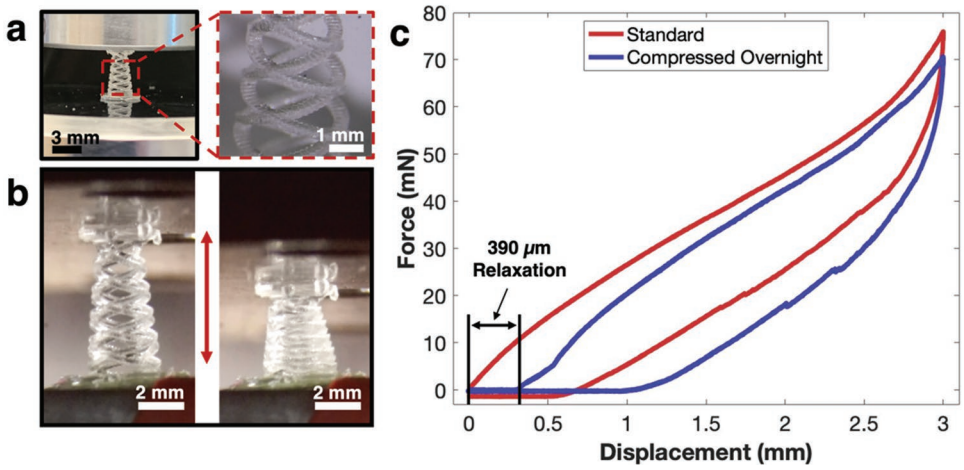

Figure 4. Mechanical aspects of the spring actuator. a) Images captured during compression testing of the spring actuator. The magnified image shows the stair like structure of the 3D printed spring that results from the layers and voxels created by the DLP printing process. b) Compression and decompression of the spring actuator during mechanical testing. c) Mean results of the mechanical test comparing one compression cycle for standard as-printed springs ($n = 8$) to springs held in compression overnight ($n = 3$). Results for standard springs were reproducible to within 5.4%, and results for overnight compression were reproducible to within 9.3%. Relaxation occurred throughout the 6 min compression cycle, and springs held in compression showed an additional 390 μm of relaxation, though the springs remained capable of extension up to 2 mm in both cases.

spring stiffness while safely interfacing with the delicate GI mucosal tissue.

3.3. Mechanical Characterization of the 3D-Printed Spring

Mechanical properties of the spring were characterized via mechanical compression tests to evaluate the spring stiffness and force application profile (**Figure 4**). Additionally, a comparison was performed between freshly printed springs and springs compressed overnight (≈18 h) to examine the impact of prolonged compression on deployment reliability. Further experimentation on the effects of compression and ageing is shown in Figure S2, Supporting Information. Samples were loaded between chucks and the springs were compressed to a displacement of 3 mm at a rate of 1 mm min^{-1}, then decompressed at 1 mm min^{-1} until reaching the origin. Force exerted on the 10 N load cell was plotted versus displacement and averaged for each group to yield the mean spring compression curves. The mean spring stiffness for each group was calculated using the maximum force, minimum force, and displacement through force loading for each sample.

The mean spring stiffness within the control group was found to be 25.4 ± 1.4 mN mm^{-1} ($n = 8$), while stiffness among the overnight compression group was 27.0 ± 2.5 mN mm^{-1} ($n = 3$). Comparing these figures to the 0.6 mN insertion force for the biomimetic barbed microneedles previously shown by Liu et al,[44,48] this force is sufficient to insert many microneedles into the GI mucosa at only small deflection values. Furthermore, the pressure exerted on the tissue at full compression, ≈24 kPa, is expected to be non-destructive to the GI tissue as previous reports of pressure application on porcine intestinal tissue showed no significant tissue trauma below 100 kPa.[55]

The use of soft polymeric materials has advantages for tissue compatibility, because the soft material is less destructive than metal springs to the delicate GI tissue. However, soft polymeric materials can exhibit viscoelastic characteristics and plastic deformation that make them challenging to use for a spring mechanism. The mechanical tests performed here give insight into the effects of viscoelastic properties on the spring actuator. The first notable consequence is that at the compression–decompression rate of 1 mm min^{-1}, the spring exhibited ≈600 μm relaxation throughout the compression. This degree of relaxation is still not prohibitive to the project objectives, as only ≈1 mm of the full 3 mm actuation distance needs to be realized for microneedle penetration into tissue. The comparison here also gives insight into the effects of long-term compression on the spring characteristics. It was observed that the overnight compression springs experience ≈390 μm of relaxation due to the prolonged compression and showed comparable relaxation to the as-printed springs during the compression cycle. Though this still enables more than the ≈1 mm actuation distance needed for SMAD anchoring, the challenge of viscoelasticity in such a soft actuator deserves more attention. In the future, selection of low-creep polymers and process refinement may significantly improve these characteristics.

3.4. Heater Characterization

Power supply for ingestible electronics is a significant limitation, and coin cells like the 2L76 are commonly used, which can produce a sustained current of up to 60 mA. Heaters were designed to maximize power dissipation under these constraints. Accordingly, the design resistance of 50 Ω limits peak current draws to ≈60 mA by ohms law with a 3.3 V source after consideration of additional internal resistances of the system. The linear dependence of conductance on cross sectional area begins to fail as material properties change below ≈100 nm trace thickness,[56] therefore the heater was designed to have the desired 50 Ω resistance with a 100 nm film deposition thickness to minimize material cost while still enabling predictable

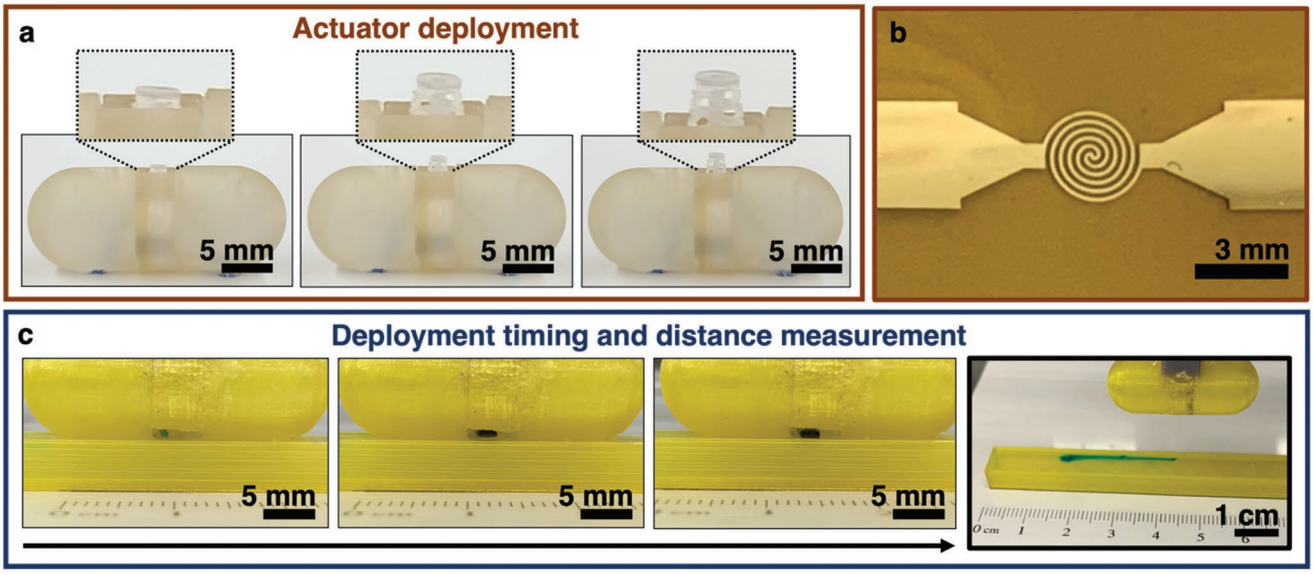

Figure 5. Releasing the actuator. a) Resistive heating element used to melt the polycaprolactone binder used to affix compression of the actuator. The heater is made of thin film (155 nm) Au deposited on a Kapton polyimide substrate. b) Demonstration of the actuation using a capsule compatible Energizer 2L76 battery regulated to 3.3 V. c) Testing of actuation distance and timing using a programmable GI motion simulator set to move at the mean translation speed in the small intestine, 1.4 cm min^{-1}. Contact with the phantom tissue surface occurred at ≈3.3 mm of translation corresponding to a time of 14.1 s ($n = 7$).

changes in resistance with changes in trace deposition thickness. Given the constraints on resistance and trace thickness, the critical parameter of trace Length $Width^{-1}$ must have the value of 208.3. Au heaters were deposited to 100 nm design trace thickness (**Figure 5**), but resistance testing revealed a systematic process error, resulting in a mean resistance of 77.5 Ω, a 55% deviation from the design value. The origin of this error is unclear; however, it could be a result of a systematic error in deposition instrumentation, lithography process, substrate topography or deposition uniformity that may have impacted the cross-sectional trace area in some regions, yielding higher than expected resistance values.

To address the deviation, a linear correction was made using the design and experimental resistance values, indicating that a 155 nm deposition thickness would return the desired 50 Ω trace resistance. The revised fabrication process was performed, yielding an experimental resistance of 49.8 ± 1.8 Ω, a 0.4% deviation from the intended resistance. The melt time of PCL when in contact with the resistive heater was evaluated by supplying current from a 2L76 coin cell battery regulated to 3.3 V. A mean melt time of 3.3 ± 0.2 s was achieved, indicating the ability of the mechanism to fire rapidly to achieve on command delivery of the drug-loaded SMAD to the GI tissue. Moreover, this melt duration at 60 mA corresponds to only 0.03% of the 2L76 160 mAh capacity.[57]

3.5. Spring Deployment Testing

Following the validation of the independent spring and heater systems under capsule-relevant constraints, the combined system was evaluated to understand characteristics of spring deployment (Figure 5). The spring actuator was deployed outside of a capsule (Figure S3, Supporting Information) and packaged in a capsule (Figure 5a) to image deployment using a 2L76 coin cell battery. Then, to determine the deployment time and distance, a capsule was translated on an intestinal simulator and the spring was fired into an agar bed. The spring was capped with a dye-loaded PVA disk, and fired at a predetermined location, eventually marking the point of contact between the dye-loaded disk and agar bed (Figure 5c). The distance between firing and dye marking was measured and the time to contact was calculated using the translation speed. The mean measured transit distance before contacting the phantom agar medium was 3.3 ± 0.7 mm ($n = 7$). Using this data and the translation speed, a deployment time of 14.1 ± 3.0 s ($n = 7$) was determined. Based on the deployment time demonstrated here and the polymer melt times, it is evident that the major contribution to deployment time is the decompression of the spring. This deployment time contribution is the experimental manifestation of the previously discussed viscoelastic spring properties. Nevertheless, spring deployment was found to be reliable and predictable, as indicated by the 3.0 s standard error in deployment time, which is acceptable relative to the mean intestinal translation speed of 1.4 cm min^{-1}.[54] Furthermore, instances of failed deployment did not occur during the controlled experiment. In early testing and development, instances of failed deployment were a result of fabrication error, for example, spring-heater misalignment, excess of PCL or poor electrical attachment to the thin-film heater—errors that would largely be resolved by mass-fabrication approaches.

The actuator deployment distance demonstrated here is an important metric to determine both the accuracy and precision of location targeting. The precision of delivery location should be high in comparison with the radius of drug spread after

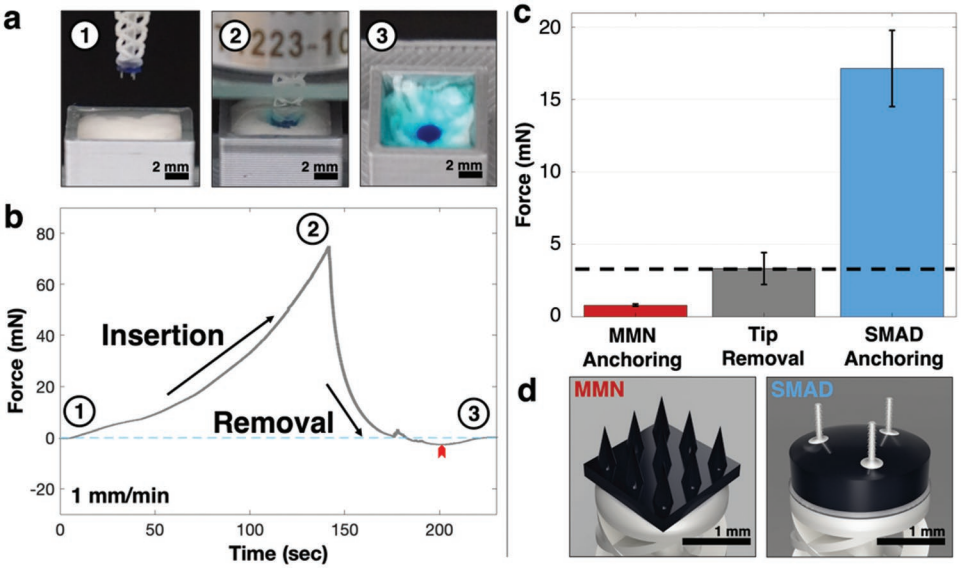

Figure 6. Mechanical testing of the SMAD. a) Images corresponding to the numbered sequence of insertion and removal. b) Example of insertion (compression) and removal (retraction) force profile throughout mechanical experiments comparing the SMAD to a traditional conical molded microneedle structure (MMN). Insertion up to 75 mN at a rate of 1 mm min^{-1} is followed by retraction until detachment of either of the structures from the actuator, or removal from the tissue. Red arrow indicates the time of peak removal force. c) Results of the force loading described in (a). SMAD demonstrated an anchoring force of 17.2 mN ($n = 4$) compared to the 0.8 mN ($n = 4$) achieved by the MMNs, a 22-fold improvement. The SMAD also reliably overcame the force required for removal from the actuator, whereas the MMNs did not sufficiently overcome this 3.3 mN ($n = 4$) force. Error bars represent standard error of the mean. SMAD anchoring, MMN anchoring and tip removal force was found to be reproducible to within 12.6%, 22.0% and 33.3%, respectively. d) CAD rendering comparing the molded microneedle (MMN) structure with the spiny microneedle anchoring drug deposit (SMAD).

delivery to ensure that the delivered drug reaches the target location. This point will be addressed below in the discussion of model drug delivery experiments. Another significant consideration is the locational accuracy, or mean deployment distance, compared to the size of the ingestible capsule. For sensor-informed delivery to locations of interest, the accuracy of drug delivery location can be augmented by the positioning of sensors in front of the drug delivery actuator to correct for the deployment distance. The Food and Drug Administration (FDA) recommended 22 mm maximum capsule size[58] is significantly larger than the 3.3 mm deployment translation distance shown here, therefore sensor placement can be used to account for the deployment time, yielding much higher accuracy in delivery. These calculations rely on the mean translation speed in the GI tract, however motion in the GI tract is not continuous, thus a more comprehensive evaluation of delivery timing could improve the precision of delivery. With sensing modalities like optical sensing, one can even estimate the current translation speed and fire the actuator at a suitable time to improve locational accuracy.

3.6. Characterization of SMAD Anchoring in Ex Vivo Tissue

To quantitatively evaluate the axial tensile removal properties of the SMAD when compared to the widely demonstrated MMN technology,[59–67] mechanical removal experiments were performed on the SMAD and MMNs attached to the spring actuator. **Figure 6**a shows a representative sample at each stage of testing, and Figure 6b illustrates the force loading and unloading during experimentation, including a red arrow indicating the point of detachment or removal. Figure 6c,d shows the mechanical removal and tip detachment data of the SMAD compared to MMNs and the corresponding renderings of each structure. 'Tip detachment force' refers to the removal force of the SMAD or MMN structure from atop the actuator, while 'anchoring force' refers to the force required to remove the SMAD or MMN structure from the tissue sample. The conical MMNs showed an anchoring force of 0.8 ± 0.1 mN ($n = 4$) compared to the 17.2 ± 2.6 mN ($n = 4$), a 22-fold improvement over the conical MMNs. Furthermore, the 17.2 mN anchoring force of the SMAD is significantly higher than the 3.3 ± 1.1 mN ($n = 4$) force required to detach the tip structure from the actuator. Conversely, the MMNs demonstrated an anchoring force that was insufficient to remove the array from the actuator. In all cases, we found that tissue removal or SMAD/MMN removal occurred before rupture of the spring. The firm tissue anchoring achieved here is critical for removal of the SMAD from the actuator, but it also enables robust adherence to the target region and, consequently, reliable prolonged therapeutic delivery. The exceptional anchoring ability of the structure demonstrated here compared to the MMNs generates more reliable tissue anchoring and system operation. Furthermore, the biocompatibility of the IP-S microneedles, Epoxy resin, PVA, and PEG materials enables prolonged attachment without significant harm to tissue and surrounding organs.

3.7. Model Drug Delivery

To demonstrate the efficacy of drug delivery in agarose phantom tissue, the diffusion of a model drug (FD&C Blue #1 Dye) from

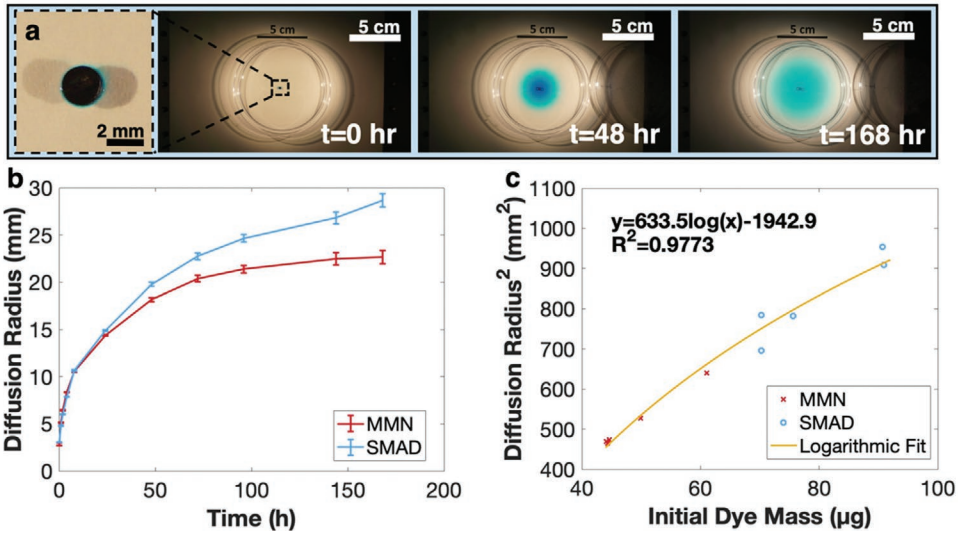

Figure 7. Quantification of model drug delivery in agarose phantom tissue. a) Diffusion of dye from a SMAD at representative time points between 0 and 168 h in a light-controlled environment. b) Diffusion radius from SMAD and MMN samples at each imaged time point. Quantitative data is obtained by MATLAB image analysis, as can be found in Figure S4, Supporting Information, with dye spread images. c) Logarithmic fit of squared diffusion radius with respect to the initial dye mass in each sample. This relationship is predicted by the diffusion equation and indicates comparable performance between the MMN group and SMAD group.

SMAD and MMN samples was compared. **Figure 7**a shows the release and subsequent diffusion of dye from a SMAD sample at 0, 48, and 168 h as representative time points for the dye diffusion profile. At 48 h, the apparent perimeter of dye diffusion is at a radial distance of ≈1.8 cm, while this expands to ≈2.5 cm after 168 h. Five samples of each SMAD and MMN were characterized using this diffusion approach and represented quantitatively as the mean diffusion radius at each measured time point in Figure 7b. Upon initial observation, there exists a discrepancy between the extent of diffusion from the MMN and SMAD. However, a difference in outcomes is to be expected due to variations in initial dye mass between MMN and SMAD structures. The thin agarose diffusion medium constrains diffusion to two dimensions; thus, this case most closely resembles 2D Fickian diffusion. The time-dependent concentration profile pertaining to this diffusion case is described by Equation (1), where C is concentration, C_0 is initial concentration, D is the diffusion constant in the given medium, t is time and r is radial distance:

$$C = C_0 \frac{1}{\sqrt{4\pi D t}} e^{-\frac{r^2}{4Dt}} \tag{1}$$

The extent of diffusion from each sample can be measured by the radial diffusion distance at which the dye concentration exceeds a threshold value. With consistent lighting, the threshold concentration value corresponds to a constant light intensity value in the dye spreading image. Thus, the red channel light intensity from a blue dye sample can be used as a direct indicator of the perimeter of constant dye concentration—enabling a quantitative treatment of the diffusion to account for differences in initial dye content across samples. For a given intensity threshold (T), the squared radial diffusion distance (r^2) is predicted by Equation (2):

$$r^2 = 4Dt\left(\ln(C_0) - \ln\left(2T(\pi Dt)^{\frac{1}{2}}\right)\right) \tag{2}$$

At one specific measurement time, D, t, and T are constant and r^2 carries a logarithmic dependence on the initial concentration; therefore, one time point can be used to compare the relationship between r^2 and C_0 for the SMAD and MMN cases. Figure 7c uses t = 168 h to compare the radial diffusion distance with initial dye mass in the context of Equation (2). The data across both groups obeys the equation with R^2 = 0.9773. To validate the logarithmic character, a diffusion coefficient of D = 2.6 × 10^{-10} m^2 s^{-1} was calculated from the logarithmic coefficient using Equation (2). This value is in strong agreement with previously reported values for the diffusion of dye in agar gel (D = [2.5 ± 0.2] × 10^{-10} m^2 s^{-1}),[68] corroborating the logarithmic data trend. These results indicate that the SMAD is capable of effusion of drug into tissue in a comparable manner to penetrating MMNs that have been widely validated in literature.

Revisiting the spread radius of dye in the agarose phantom, the radius of dye spread in tissue is a critical parameter because containment enables increased local concentration with reduced dosing. However, radial diffusion distance must be sufficient to target an inflammatory location with high repeatability using the actuation mechanism demonstrated here. The intestinal translation distance between firing and tissue contact varied with a standard error of 0.7 mm and a 99.9% confidence level of repeatability within 2.24 mm. Compared to the dye spread radius demonstrated in Figure 7 of up to 25 mm, the repeatability is more than sufficient to ensure therapeutic coverage to the inflammatory target site. Moreover, there is room to increase the localization, which can be done using material selection. The expulsion of model drug from the drug disk relies primarily on the diffusion of a dye from the PVA following the

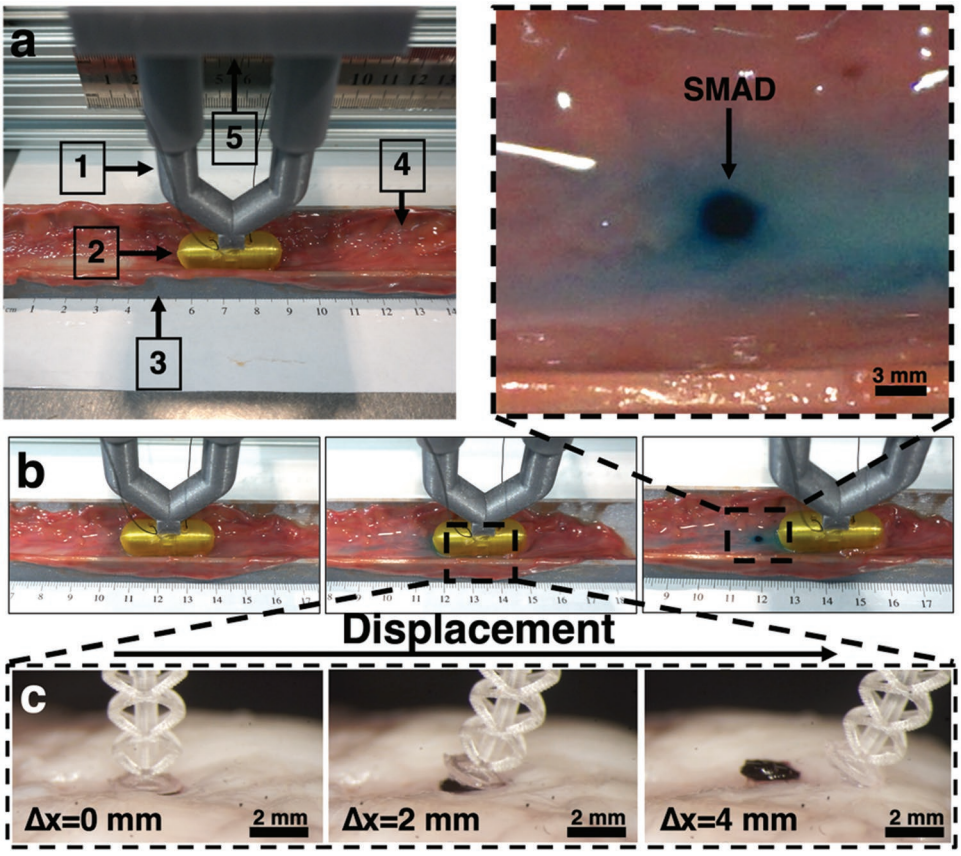

Figure 8. Evaluation of the packaged SMAD and actuator in ex vivo tissue. a) Ex vivo testing apparatus composed of: i) a vertical slider that transfers a relevant load to the test capsule; ii) a test capsule; iii) a 3D-printed PLA tissue holder with an inner radius of curvature of 12.5 mm; iv) ex vivo intestinal tissue; and v) the translating device to control motion of the test capsule. b) Firing of the spring actuator and SMAD into intestinal tissue on command. There is no noticeable dye leaking out of the capsule opening before actuation, however after actuation, the SMAD is left behind in tissue to deliver model therapeutic agent to the local area in the tissue. c) Lateral removal of the SMAD in ex vivo intestinal tissue showing removal after ≈3 mm of spring deflection.

polymer hydration and swelling. Once hydrated, the diffusion from the SMAD to the phantom tissue is rapid compared to diffusion through the phantom and the concentration in the SMAD is approximately equal to the directly adjacent phantom. In this sense, the disk acts as a directly connected reservoir of therapeutic agent, thus the drug spread relies largely on diffusion from the SMAD. Alternatively, low-solubility materials could be used that would offer the ability to regulate and significantly slow the release of drug from the SMAD. Consequently, the system developed here provides a platform for modulating the release profile utilizing a variety of materials with different dissolution or swelling rates in intestinal fluid to fit the needs of the desired application, potentially spanning to broader applications than only gastrointestinal inflammation.

3.8. Spring Deployment and SMAD Release in Tissue

To demonstrate the combined system operation in a controlled ex vivo environment, the entire packaged system was placed in a test capsule and fired into porcine intestinal tissue (**Figure 8**). Power was supplied to the heater and limited to 3.3 V and 60 mA, emulating capsule conditions. Translation on the ex vivo tissue occurred at a speed of 1.4 cm min^{-1}, and the spring was fired during translation. No leakage of dye into the tissue and surrounding fluid was observed before the SMAD was released into the tissue. Following the deployment of the actuator, blue dye could be seen behind the capsule, then the SMAD appeared from behind the capsule. This result validates the reliable location-specific release that the actuator and SMAD can achieve. Notably, the presence of simulated intestinal fluid media increases the rate of drug spread and impacts the level of achievable localization. Further investigation will be required to understand the degree of drug spread with varying drug disk composition and intestinal fluidic conditions. Nevertheless, the prolonged direct tissue contact made by the SMAD enables the greatly increased localization of effused drug when compared to an instantaneous release of fluid.

Throughout deployment a significant component of displacement and force on the system will be applied perpendicular to the actuation direction. To model and document SMAD release in this case, the SMAD was attached to an actuator outside of a capsule, applied to tissue and translated laterally (Figure 8c) until the SMAD structure was removed. Removal occurred at ≈3 mm deflection, corresponding to 3 mm of capsule transit within the intestine. This experiment further validates the structures removal in tissue under lateral force application and gives insight into the removal characteristics.

Overall, the significantly localized model drug delivery achieved using the SMAD has the potential to considerably increase the level of focused treatment for early intervention of GI disorders. Directed therapeutic delivery to the 2.5 cm delivery radius demonstrated here compared to the ≈32 m^2 gastrointestinal surface area[69] would result in a ≈16 000-fold higher areal drug concentration. This drastic enhancement in local concentration could serve to mitigate or effectively eliminate drug side effects with lower dosing and achieve enhanced targeted treatment of affected inflammatory regions, enabling early intervention of GI disorders, and limiting the spread and consequences of the disease while minimizing drug side effects.

It is critical to note that the localization of drug release could vary significantly when performed in vivo. The introduction of peristaltic and segmentation movements,[70] as well as varying fluid and mucus content will result in lower predictability in delivery localization. Still, location specific delivery is significantly enhanced using this mechanism. There are also tissue compatibility challenges within the dynamic GIT environment. The SMAD has the potential to become permanently lodged within tissue via envelopment in intestinal folds, which could lead to complications including blockage and infection. One mitigating circumstance is the solubility of the drug disk, resulting in complete dissolution on the scale of days, leaving only the microscale biocompatible needles to be cleared by cellular mucosal cell turnover.[71] Further experimentation is also needed to evaluate the impacts of prolonged retention on tissue integrity and inflammation, as well as blockage for passing luminal contents including the capsule itself. Microneedle devices in general have been established as exhibiting low tissue damage,[59,60,65] however more analysis is needed to evaluate the impacts of the biomimetic needles on tissue. Nevertheless, the system demonstrated here has the potential to meaningfully enrich the collection of available targeted drug delivery technologies.

The hybrid fabrication process demonstrated here utilizes several technologies in concert to achieve precise actuation and robust anchoring. Scaling of these processes also presents a challenge, as 3D printing methods in particular are of notoriously low throughput. However, micromolding of 3D printed components from this proof-of-concept system presents a possible mass scale fabrication strategy that would further enable versatility in material selection. Fabrication reliability and throughput would also be augmented by robotic assembly machines for film casting, stamping, microfabrication, and component placement. Evaluating the aptitude of such large-scale processes will be a critical investigation for future application of this technology.

4. Conclusion

In this paper we introduce a compact thermomechanical 3D-printable actuator combined with the first application of biomimetic barbed microneedles toward drug delivery in the GI tract. This is accomplished using a 50 Ω microfabricated thin film Au resistive heating element that melts a PCL adhesive layer, firing the spring actuator. Gastrointestinal anchoring is achieved by a SMAD structure, composed of spiny microneedles adhered to a dissolving drug loaded PVA deposit. The high resolution (≈1 μm) of the DLW process enables high sharpness and a firm tissue anchoring force of 17.2 ± 2.6 mN (n = 4). The actuator demonstrated reliable and repeatable deployment with a mean deployment time of 14.1 ± 3.0 s (n = 7), and SMADs with the barbed microneedles anchored with a 22-fold higher tissue retention force than conical molded microneedles—reliably overcoming the force required for removal of the SMAD from the spring actuator. SMADs also demonstrated comparable drug delivery characteristics to standard MMNs through model drug delivery in an agarose phantom tissue. Diffusion of dye from SMADs reached a radial distance of 25 mm. After correction for the initial dye mass in each sample, the SMAD and MMN data showed high correlation (R^2 = 0.9773) indicating predictable and comparable performance with a diffusion constant of D = 2.6×10^{-10} m^2 s^{-1}. Furthermore, the vast material selection available for a simple disk structure introduces a means for direct modulation of drug release profiles and spread characteristics. Overall, the reliable actuation and robust anchoring provided by this system enables location-specific long-term delivery and anchoring of therapeutics to facilitate prolonged treatment of target locations in the GI tract, opening new possibilities for early therapeutic treatment of GI diseases and other local gastrointestinal conditions.

Supporting Information

Supporting Information is available from the Wiley Online Library or from the author.

Acknowledgements

This work was supported by the National Science Foundation ECCS Program under Award #1939236. The authors also acknowledge support from the Clark Doctoral Fellows Program, TerrapinWorks, the University of Maryland NanoCenter and its FabLab.

Conflict of Interest

The authors declare no conflict of interest.

Data Availability Statement

The data that support the findings of this study are available from the corresponding author upon reasonable request.

Keywords

biomimetic, digital light processing, direct laser writing, drug delivery, ingestible device, localized, thermomechanical actuator

Received: August 19, 2022
Revised: October 11, 2022
Published online: December 4, 2022

[1] "People with IBD Have More Chronic Diseases | CDC," can be found under https://www.cdc.gov/ibd/features/IBD-more-chronic-diseases.html (accessed: July 2022).
[2] W. Strober, I. Fuss, P. Mannon, *J. Clin. Invest.* **2007**, *117*, 514.
[3] "What is inflammatory bowel disease (IBD)? | IBD," can be found under https://www.cdc.gov/ibd/what-is-IBD.htm (accessed: July 2022).
[4] K. E. Trinkley, M. C. Nahata, *J. Clin. Pharm. Ther.* **2011**, *36*, 275.
[5] M. S. Alqahtani, M. Kazi, M. A. Alsenaidy, M. Z. Ahmad, *Front. Pharmacol.* **2021**, *12*, 62.
[6] A. B. Pithadia, S. Jain, *Pharmacol. Rep.* **2011**, *63*, 629.
[7] S. B. Hanauer, D. H. Present, *Rev. Gastroenterol. Disord.* **2003**, *3*, 81.
[8] C. N. Bernstein, *Am. J. Gastroenterol.* **2015**, *110*, 114.
[9] A. Stallmach, S. Hagel, T. Bruns, *Best Pract. Res. Clin. Gastroenterol.* **2010**, *24*, 167.
[10] H. Nguyen, A. K. Bakshi, A. S. Kashyap, M. L. Borum, *J. Clin. Gastroenterol.* **2009**, *43*, 694.
[11] R. B. Stein, S. B. Hanauer, *Drug Saf.* **2000**, *23*, 429.
[12] T. Ali, D. Lam, M. S. Bronze, M. B. Humphrey, *Am. J. Med.* **2009**, *122*, 599.
[13] "Crohn's Disease Treatment: Medications, Options, and More," can be found under https://www.healthline.com/health/crohns-disease/medications#medications (accessed: June 2022).
[14] J. A. Fishman, *Cold Spring Harbor Perspect. Med.* **2013**, *3*, a015669.
[15] P. Eder, A. Zielińska, J. Karczewski, A. Dobrowolska, R. Słomski, E. B. Souto, *J. Nanobiotechnol.* **2021**, *19*, 346.
[16] B. Gareb, A. T. Otten, H. W. Frijlink, G. Dijkstra, J. G. W. Kosterink, *Pharmaceutics* **2020**, *12*, 539.
[17] U. Klotz, M. Schwab, *Adv. Drug Delivery Rev.* **2005**, *57*, 267.
[18] M. Widjaja, J. Gan, J. S. R. Talpaneni, R. R. Tjandrawinata, *Sci. Pharm.* **2018**, *86*, 38.
[19] J. Fallingborg, L. A. Christensen, M. Ingeman-Nielsen, B. A. Jacobsen, K. Abildgaard, H. H. Rasmussen, S. N. Rasmussen, *J. Pediatr. Gastroenterol. Nutr.* **1990**, *11*, 211.
[20] C. G. M. Gennari, P. Sperandeo, A. Polissi, P. Minghetti, F. Cilurzo, *J. Pharm. Sci.* **2019**, *108*, 3667.
[21] B. M. Boddupalli, Z. N. K. Mohammed, R. A. Nath, D. Banji, *J. Adv. Pharm. Technol. Res.* **2010**, *1*, 381.
[22] J. Byrne, H. W. Huang, J. C. McRae, S. Babaee, A. Soltani, S. L. Becker, G. Traverso, *Adv. Drug Delivery Rev.* **2021**, *177*, 113926.
[23] A. Abramson, E. Caffarel-Salvador, M. Khang, D. Dellal, D. Silverstein, Y. Gao, M. R. Frederiksen, A. Vegge, F. Hubálek, J. J. Water, A. V. Friderichsen, J. Fels, R. K. Kirk, C. Cleveland, J. Collins, S. Tamang, A. Hayward, T. Landh, S. T. Buckley, N. Roxhed, U. Rahbek, R. Langer, G. Traverso, *Science* **2019**, *363*, 611.
[24] M. Hashim, R. Korupolu, B. Syed, K. Horlen, S. Beraki, P. Karamchedu, A. K. Dhalla, R. Ruffy, M. Imran, *Pharmacol. Res. Perspect.* **2019**, *7*, e00522.
[25] A. Abramson, E. Caffarel-Salvador, V. Soares, D. Minahan, R. Y. Tian, X. Lu, D. Dellal, Y. Gao, S. Kim, J. Wainer, J. Collins, S. Tamang, A. Hayward, T. Yoshitake, H. C. Lee, J. Fujimoto, J. Fels, M. R. Frederiksen, U. Rahbek, N. Roxhed, R. Langer, G. Traverso, *Nat. Med.* **2019**, *25*, 1512.
[26] "PillCamTM SB 3 System | Medtronic," can be found under https://www.medtronic.com/covidien/en-us/products/capsule-endoscopy/pillcam-sb-3-system.html (accessed: June 2022).
[27] K. Kalantar-Zadeh, K. J. Berean, N. Ha, A. F. Chrimes, K. Xu, D. Grando, J. Z. Ou, N. Pillai, J. L. Campbell, R. Brkljača, K. M. Taylor, R. E. Burgell, C. K. Yao, S. A. Ward, C. S. McSweeney, J. G. Muir, P. R. Gibson, *Nat. Electron.* **2018**, *1*, 79.
[28] K. J. Berean, N. Ha, J. Z. Ou, A. F. Chrimes, D. Grando, C. K. Yao, J. G. Muir, S. A. Ward, R. E. Burgell, P. R. Gibson, K. Kalantar-Zadeh, *Aliment. Pharmacol. Ther.* **2018**, *48*, 646.
[29] P. A. Thwaites, C. K. Yao, J. Maggo, J. John, A. F. Chrimes, R. E. Burgell, J. G. Muir, F. C. Parker, D. So, K. Kalantar-Zadeh, R. B. Gearry, K. J. Berean, P. R. Gibson, *Aliment. Pharmacol. Ther.* **2022**, *56*, 1337.
[30] C. Cheng, Y. Wu, X. Li, Z. An, Y. Lu, F. Zhang, B. Su, Q. Liu, *Sens. Actuators, B* **2021**, *349*, 130781.
[31] K. Yamasue, H. Hagiwara, O. Tochikubo, C. Sugimoto, R. Kohno, *Adv. Biomed. Eng.* **2012**, *1*, 9.
[32] H. S. Magar, R. Y. A. Hassan, A. Mulchandani, *Sensors* **2021**, *21*, 6578.
[33] J. Chandrappan, L. Ruiqi, N. Su, G. H. Y. Yi, K. Vaidyanathan, *J. Micromech. Microeng.* **2011**, *21*, 045037.
[34] W. Yu, R. Rahimi, M. Ochoa, R. Pinal, B. Ziaie, *IEEE Trans. Biomed. Eng.* **2015**, *62*, 2289.
[35] J. Cui, X. Zheng, W. Hou, Y. P. Zhuang, X. Pi, J. Yang, *Telemed. J. e-Health* **2008**, *14*, 715.
[36] P. Xitian, L. Hongying, W. Kang, L. Yulin, Z. Xiaolin, W. Zhiyu, *Int. J. Pharm.* **2009**, *382*, 160.
[37] X. Pi, Y. Lin, K. Wei, H. Liu, G. Wang, X. Zheng, Z. Wen, D. Li, *Sens. Actuators, A* **2010**, *159*, 227.
[38] R. Goffredo, D. Accoto, M. Santonico, G. Pennazza, E. Guglielmelli, *Proc. Ann. Int. Conf. IEEE Eng. Med. Biol. Soc. (EMBS)*, IEEE, Piscataway, NJ **2015**, p. 1361.
[39] J. Lee, H. Lee, S.-H. Kwon, S. Park, *Med. Eng. Phys.* **2020**, *85*, 87.
[40] T. G. Leong, C. L. Randall, B. R. Benson, N. Bassik, G. M. Stern, D. H. Gracias, *Proc. Natl. Acad. Sci. U. S. A.* **2009**, *106*, 703.
[41] K. Malachowski, J. Breger, H. R. Kwag, M. O. Wang, J. P. Fisher, F. M. Selaru, D. H. Gracias, *Angew. Chem., Int. Ed.* **2014**, *53*, 8045.
[42] A. Ghosh, L. Li, L. Xu, R. P. Dash, N. Gupta, J. Lam, Q. Jin, V. Akshintala, G. Pahapale, W. Liu, A. Sarkar, R. Rais, D. H. Gracias, F. M. Selaru, *Sci. Adv.* **2020**, *6*, 4133.
[43] A. Ghosh, W. Liu, L. Li, G. Pahapale, S. Y. Choi, L. Xu, Q. Huang, F. M. Selaru, D. H. Gracias, *bioRxiv* **2022**, 20220505490821.
[44] S. Liu, S. Chu, G. E. Banis, L. A. Beardslee, R. Ghodssi, *Proc. IEEE Int. Conf. Micro Electro Mech. Syst. (MEMS)*, IEEE, Piscataway, NJ **2020**, p. 885.
[45] D. Han, R. S. Morde, S. Mariani, A. A. la Mattina, E. Vignali, C. Yang, G. Barillaro, H. Lee, D. Han, R. S. Morde, C. Yang, H. Lee, S. Mariani, A. A. la Mattina, E. Vignali, G. Barillaro, *Adv. Funct. Mater.* **2020**, *30*, 1909197.
[46] L. G. Tran, T. Q. Nguyen, W. T. Park, *Proc. IEEE Int. Conf. Micro Electro Mech. Syst. (MEMS)*, IEEE, Piscataway, NJ **2019**, p. 547.
[47] Z. Chen, Y. Lin, W. Lee, L. Ren, B. Liu, L. Liang, Z. Wang, L. Jiang, *ACS Appl. Mater. Interfaces* **2018**, *10*, 29338.
[48] S. Liu, S. Chu, L. A. Beardslee, R. Ghodssi, *J. Microelectromech. Syst.* **2020**, *29*, 706.
[49] A. Zolfagharian, A. Kaynak, S. Y. Khoo, A. Z. Kouzani, *3D Print. Addit. Manuf.* **2018**, *5*, 138.
[50] V. P. Anju, R. Pratoori, D. K. Gupta, R. Joshi, R. K. Annabattula, P. Ghosh, *Soft Matter* **2020**, *16*, 4162.
[51] A. Dallinger, P. Kindlhofer, F. Greco, A. M. Coclite, *ACS Appl. Polym. Mater.* **2021**, *3*, 1809.
[52] O. M. Amin, R. A. Heckmann, N. Van Ha, *Parasite* **2014**, *21*, 53.
[53] J. Cutnell, K. Johnson, *Physics*, 4th ed., John Wiley & Sons, Inc., **1998**.
[54] L. Barducci, J. C. Norton, S. Sarker, S. Mohammed, R. Jones, P. Valdastri, B. S. Terry, *Prog. Biomed. Eng.* **2020**, *2*, 042002.
[55] A. F. Khan, M. K. Macdonald, C. Streutker, C. Rowsell, J. Drake, T. Grantcharov, *BMJ Surg. Interventions Health Technol.* **2021**, *3*, e000084.
[56] T. H. Gilani, D. Rabchuk, *Can. J. Phys.* **2018**, *96*, 272.
[57] "Energizer 2L76 Product Datasheet," can be found under https://data.energizer.com/pdfs/2l76.pdf (accessed: August 2022).
[58] V. Sayeed, *Size, Shape, and Other Physical Attributes of Generic Tablets and Capsules Guidance for Industry, US Food and Drug Administration* **2015**, https://www.fda.gov/Drugs/GuidanceComplianceRegulatoryInformation/Guidances/default.htm (accessed: June 2022).

[59] M. R. Prausnitz, *Adv. Drug Delivery Rev.* **2004**, *56*, 581.
[60] J. W. Lee, J. H. Park, M. R. Prausnitz, *Biomaterials* **2008**, *29*, 2113.
[61] H. S. Gill, M. R. Prausnitz, *J. Controlled Release* **2007**, *117*, 227.
[62] J. H. Park, M. G. Allen, M. R. Prausnitz, *Pharm. Res.* **2006**, *23*, 1008.
[63] L. E. Moore, S. Vucen, A. C. Moore, *Eur. J. Pharm. Biopharm.* **2022**, *173*, 54.
[64] S. Liu, M. N. Jin, Y. S. Quan, F. Kamiyama, K. Kusamori, H. Katsumi, T. Sakane, A. Yamamoto, *Eur. J. Pharm. Biopharm.* **2014**, *86*, 267.
[65] J. H. Park, M. G. Allen, M. R. Prausnitz, *J. Controlled Release* **2005**, *104*, 51.
[66] T. Miyano, Y. Tobinaga, T. Kanno, Y. Matsuzaki, H. Takeda, M. Wakui, K. Hanada, *Biomed. Microdevices* **2005**, *7*, 185.
[67] S. P. Davis, B. J. Landis, Z. H. Adams, M. G. Allen, M. R. Prausnitz, *J. Biomech.* **2004**, *37*, 1155.
[68] T. Støren, A. Simonsen, O. J. Løkberg, L. O. Svaasand, A. Røyset, T. Lindmo, *Opt. Lett.* **2003**, *28*, 1215.
[69] H. F. Helander, L. Fändriks, *Scand J Gastroenterol* **2014**, *49*, 681.
[70] K. S. Patel, A. Thavamani, *Physiology, Peristalsis*, StatPearls Publishing, (accessed: October 2022).
[71] B. Creamer, *Br. Med. Bull.* **1967**, *23*, 226.